PAPER

Check for updates

Giant enhancement of anti-quenching upconversion luminescence in $Sc_2W_3O_{12}$:Er^{3+}/Yb^{3+} phosphors for temperature sensing†

Xufang Wang,[a] Ping Zhang,[a] Xianglong Xiao,[a] Ruoshan Lei,[a] Lihui Huang,[a] Shiqing Xu,[a] Shilong Zhao [ID] *[a] and Xiuli Wang*[b]

Although negative thermal expansion (NTE) materials provide a new strategy to overcome the thermal-quenching phenomenon among rare earth doped luminescent materials, the overall weak upconversion luminescence still restricts their application in the field of optical temperature sensing. Herein, giant enhancement of anti-quenching upconversion luminescence is achieved in the NTE $Sc_2W_3O_{12}$:Er^{3+}/Yb^{3+} phosphors by $(KMg)^{3+}$ impurity doping, and the phosphors are used for the construction of an all-fiber temperature sensing (AFTS) system. Compared to the upconversion luminescence of the $Sc_2W_3O_{12}$:Er^{3+}/Yb^{3+} phosphors at room temperature, the synergistic effect of impurity doping and NTE characterstics results in a 6000-fold enhancement of the upconversion luminescence of the $(KMg)^{3+}$ doped $Sc_2W_3O_{12}$:Er^{3+}/Yb^{3+} phosphors at 573 K. A single-point tip temperature sensor was constructed based on the fluorescence luminescence intensity ratio (FIR) technology and the corresponding self-calibrated curves were obtained with a regression coefficient of 0.9996. The potential application of the constructed AFTS system was demonstrated in the real-time temperature monitoring of a CPU chip and a thermostat bath.

1 Introduction

Optical materials have drawn much attention due to their strong resistance to electromagnetic interference, high signal resolution, and adaptation to complex environments.[1,2] The FIR technique on the basis of the fluorescence intensity ratios of two thermally coupled energy levels of rare-earth ions at different temperatures has become a hot spot among many optical temperature measurement techniques due to its high accuracy and sensitivity.[3,4] However, the common thermal quenching (TQ) phenomenon of optical materials limits their application in the high temperature range.[5,6] Hence, maintaining or even enhancing the luminescence intensity at high temperature is of great significance.

In recent years, great efforts were devoted to develop anti-thermal quenching luminescence materials and $A_2M_3O_{12}$ (A-Trivalent ions, M = Mo, W) materials with negative thermal

expansion (NTE) characteristics attracted great attention. As the temperature increases, the contraction of the $A_2M_3O_{12}$ lattice leads to a decrease of the distance between the activated ions, which enhances the energy transfer efficiency and luminescence intensity. A 21-fold enhancement of green luminescence in $Yb_{1.98}Er_{0.02}Mo_3O_{12}$ microcrystals was achieved from 313 to 573 K.[7] Green upconversion luminescence was selectively thermally enhanced 54-fold from 298 K to 523 K in $Y_2Mo_3O_{12}$:Yb^{3+}/Er^{3+} phosphors.[8] In Er^{3+}/Yb^{3+} co-doped $Sc_2W_3O_{12}$ phosphors, the overall upconversion luminescence intensity at 753 K was 74.5 times higher than that at room temperature.[9] Unfortunately, in order to obtain strong upconversion luminescence, the excitation power still needs to be maintained at a high level (2–3 W cm⁻²). Thus, the laser thermal effect is inevitable, and is very likely to cause a local temperature increase and reduce the accuracy of temperature sensing devices.[10] The key to developing high-performance temperature sensing materials is further enhancing their upconversion luminescence performance while simultaneously maintaining their NTE characteristics at high temperature.

In the $A_2M_3O_{12}$ materials, the composition of A-site ions affects the NTE and other properties.[11,12] Isovalent (Al^{3+}, Fe^{3+}) and heterovalent (Li^+/Mg^{2+} combination) ion doping methods have been used to optimize the NTE performance of $A_2M_3O_{12}$ materials and reduce hygroscopicity.[13–15] Moreover, the

[a] *Key Laboratory of Rare Earth Optoelectronic Materials and Devices of Zhejiang Province, Institute of Optoelectronic Materials and Devices, China Jiliang University, Hangzhou 310018, China. E-mail: zhaosl75@cjlu.edu.cn*

[b] *College of Materials, Chemistry and Chemical Engineering, Hangzhou Normal University, Hangzhou 311121, China. E-mail: xlwanghx@hotmail.com*

† Electronic supplementary information (ESI) available. See DOI: https://doi.org/10.1039/d4tc01673d

This journal is © The Royal Society of Chemistry 2024

J. Mater. Chem. C, 2024, **12**, 8977–8986 | 8977

impurity doping is also extensively adopted to adjust the local symmetry and improve the photoluminescence performance of active ions. Tens of times upconversion luminescence enhancement was achieved by impurity doping.[16–18] To our knowledge, there have been no reports on the simultaneous optimization of the thermal expansion performance of $A_2M_3O_{12}$ materials and the luminescence performance of activated ions using impurity doping. $Sc_2W_3O_{12}$, as a member of the $A_2M_3O_{12}$ family, has the widest NTE response interval available and exhibits excellent NTE properties.[19–22] In this work, the dependence of structural evolution and luminescence enhancement on the impurity doping $(KMg)^{3+}$ was investigated in rare earth doped $Sc_2W_3O_{12}$ phosphors. The reduced local symmetry and the maximum phonon-energy, high crystallinity and high energy transfer efficiency result in a great enhancement of upconversion luminescence. The new solid solution phase $K_{0.6}Mg_{0.6}Sc_{1.4}Mo_3O_{12}$:$Er^{3+}/Yb^{3+}$ phosphors retain their NTE properties and exhibit anomalous thermal enhancement. A FIR-based all-fiber temperature sensor was fabricated and used for the real-time temperature monitoring of a CPU chip and a thermostat bath.

2 Experimental section

2.1 Sample preparation

A high temperature sintering method was used to fabricate rare-earth doped $(KMg)_{2-x}Sc_xW_3O_{12}$ phosphors. $(KMg)_xSc_{2-x}W_3O_{12}$:1 mol% Er^{3+}/20 mol% Yb^{3+} (x = 0, 0.25, 0.5, 0.6, 0.75, 1, and 1.25), $(KMg)_ySc_{2-y}W_3O_{12}$:1 mol% Eu^{3+} (y = 0, 0.25, 0.5, 0.75, 1, and 1.25), $(KMg)_zSc_{2-z}W_3O_{12}$ (z = 0, 0.25, 0.5, 0.6, 0.75, 1, and 1.25), $(KMg)ScW_3O_{12}$:a mol% Er^{3+}/20 mol% Yb^{3+} (a = 0.5, 1, 1.5, 2, and 3) and $(KMg)ScW_3O_{12}$:2 mol% Er^{3+}/b mol% Yb^{3+} (b = 10, 15, 20, 25, 30, and 35) with different stoichiometric molar ratios were designed. The raw materials are high-purity tungsten trioxide (WO_3), scandium oxide (Sc_2O_3), magnesium oxide (MgO), potassium carbonate (K_2CO_3), europium oxide (Eu_2O_3), erbium oxide (Er_2O_3) and yttrium oxide (Yb_2O_3). All materials are weighed and mixed well and then transferred to the Max 10 Transparent Cup. Anhydrous ethanol was added to the mixture and mixed using a Hauschild SpeedMixer 3 times for 5 minutes each time. After drying at 353 K, the mixed slurry was further ground using an agate mortar for 20 minutes and pre-fired at 873 K for 6 hours. Finally, the mixture was pressed into $\Phi 8 \times 2$ mm discs and sintered at 1123 K for 8 hours.

2.2 Instruments and characterization

A Bruker D2 PHASER X-ray diffractometer (XRD) (Germany), a Renishaw InVia Raman microscope (U.K.), a Hitachi scanning electron microscope (SEM) (Japan), a Tecnai G2 F20 transmission electron microscope (TEM) (Holland), a Horiba Jobin-Yvon Fluorolog-3 fluorescence spectrometer (France), and a thermomechanical analyzer (TMA) (TA TMAQ400, America) were used. High-temperature XRD patterns were recorded on the Nihon Riken-Rigaku/SmartLab SE XRD.

3 Results and discussion

The XRD patterns of the Er^{3+}/Yb^{3+} co-doped $(KMg)_xSc_{2-x}W_3O_{12}$ (x = 0, 0.25, 0.5, 0.6, 1, 0.75, and 1.25) phosphors are shown in Fig. 1. When x = 0, a pure orthorhombic $Sc_2W_3O_{12}$ phase was obtained and all diffraction peaks coincided well with JCPDS 21-1065. Due to the same valence and similar ionic radius, Er^{3+} and Yb^{3+} ions preferentially occupy the position of Sc^{3+} ions. With the substitution of $(KMg)^{3+}$ ions for Sc^{3+} ions, a new hexagonal $K_{0.6}Mg_{0.6}Sc_{1.4}Mo_3O_{12}$ (JCPDS 47-0747) phase appears. When x is between 0.5 and 1, a pure hexagonal $(KMg)_xSc_{2-x}W_3O_{12}$ phosphor was obtained. Further substitution (x = 1.25) produces new diffraction peaks, which correspond to the monoclinic $MgWO_4$ (JCPDS 27-0789) phase.

The crystallographic structure of orthorhombic $Sc_2W_3O_{12}$ and hexagonal $(KMg)_xSc_{2-x}W_3O_{12}$ is shown in Fig. 2(a) and (b). $Sc_2W_3O_{12}$ consists of ScO_6 octahedra and WO_4 tetrahedra connected by common vertices. Er^{3+}/Yb^{3+} ions occupy the sites of Sc^{3+} ions with C_1 (8d) symmetry.[23] Hexagonal $(KMg)_xSc_{2-x}W_3O_{12}$ is also consisted of co-vertex ScO_6 octahedra and WO_4 tetrahedra. The random substitution of Mg^{2+} and Er^{3+}/Yb^{3+} for Sc^{3+} leads to a further decrease of lattice symmetry. K^+ ions fill in the channels constructed from the WO_4 tetrahedra and $[(Mg/Sc)O_6]$ octahedra. In order to investigate the influence of $(KMg)^{3+}$ impurity doping on the crystal structure, the XRD patterns were refined and displayed in Fig. S1 (ESI†). Fig. 2(c) shows the average bond length of K–O, Mg/Sc–O, W–O in the KO_6 octahedra, $[(Mg/Sc)O_6]$ octahedra and WO_4 tetrahedra, respectively. With the gradual substitution of $(KMg)^{3+}$ for Sc^{3+}, a continuous shortening of the average bond length for Sc/Mg–O and W–O is observed, while the average bond length of K–O increases continuously from 2.822 to 2.826 Å. Due to the

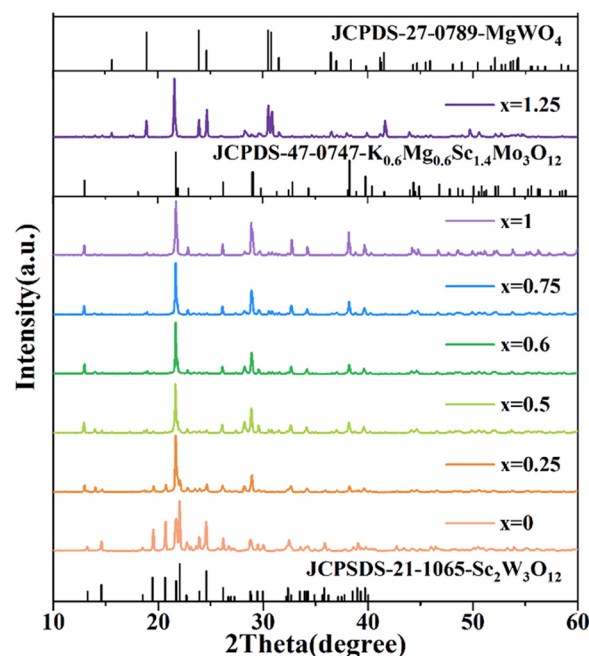**Fig. 1** XRD patterns of the $(KMg)_xSc_{2-x}W_3O_{12}$:1 mol% Er^{3+}/20 mol% Yb^{3+} (x = 0, 0.25, 0.5, 0.6, 0.75, 1, and 1.25) phosphors.
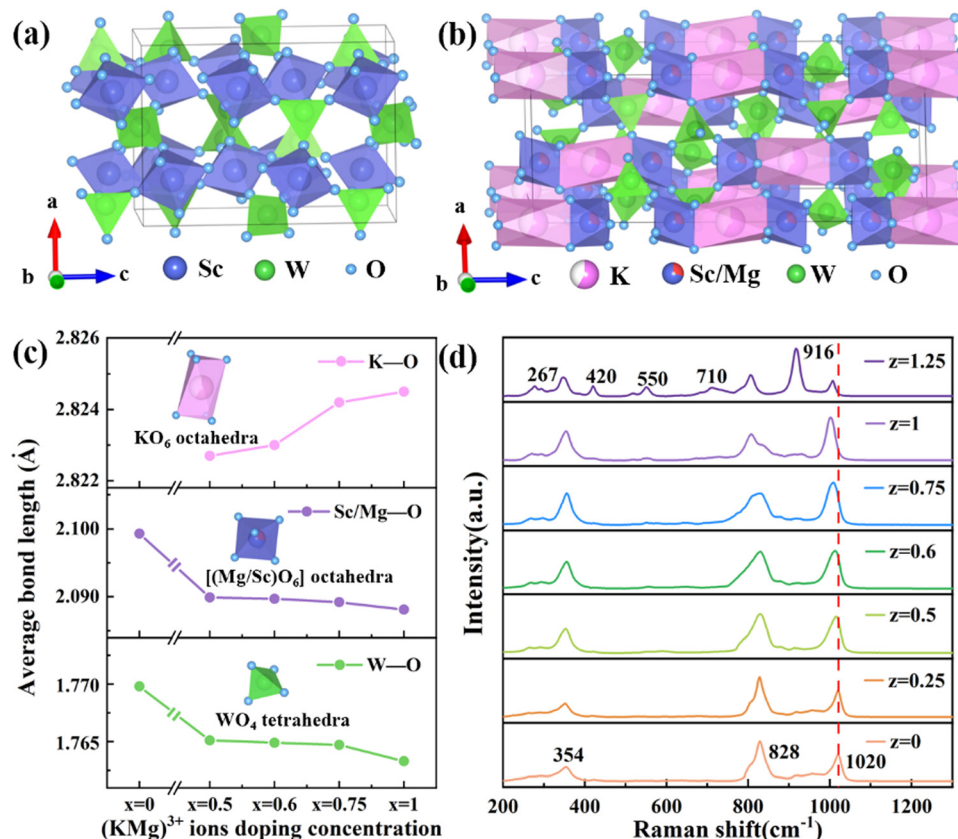
8978 | *J. Mater. Chem. C*, 2024, **12**, 8977–8986

This journal is © The Royal Society of Chemistry 2024

Fig. 2 Crystallographic structure of (a) orthorhombic $Sc_2W_3O_{12}$ and (b) hexagonal $(KMg)_xSc_{2-x}W_3O_{12}$. (c) The influence of $(KMg)^{3+}$ ion doping on the average bond length of K–O, Mg/Sc–O and W–O bonds. (d) Raman spectra of $(KMg)_zSc_{2-z}W_3O_{12}$ phosphors.

large ionic radius of K^+, KO_6 octahedra will expel the surrounding WO_4 tetrahedra and $[(Mg/Sc)O_6]$ octahedra. With a gradual increase of the K^+ doping concentration, WO_4 tetrahedra and $[(Mg/Sc)O_6]$ gradually contract, which lead to the shortening of W–O and Mg/Sc–O bond lengths. Moreover, the smaller ionic radius of Mg^{2+} ions further shortens the Mg/Sc–O bond. Thus, the lattice distortion of the $[(Mg/Sc)O_6]$ unit leads to a further reduction of local symmetry, which is very beneficial for improving upconversion luminescence.[24,25]

The influence of impurity doping on the structural evolution was further investigated using the Raman spectra shown in Fig. 2(d). For $Sc_2W_3O_{12}$, the characteristic Raman peaks appear at 1020, 828 and 354 cm^{-1}, which are assigned to the symmetric and asymmetric stretching vibrations of the WO_4 tetrahedra, as well as the symmetric and asymmetric bending vibrations of ScO_6 octahedra and WO_4 tetrahedra, respectively.[26] As $(KMg)^{3+}$ ions gradually substitute for Sc^{3+} ions, an obvious red shift was observed in the above Raman peaks. It is believed that the distortion of polyhedra and stress introduced by gradual substitution of $(KMg)^{3+}$ for Sc^{3+} ions in the unit cell are responsible for these changes.[27] Obviously, the remarkable red shift of Raman peaks brings a decrease in the maximum phonon energy,[28] which is very beneficial to achieve strong luminescence of rare-earth ions.

Fig. 3 presents the morphology of $(KMg)_xSc_{2-x}W_3O_{12}$: 1 mol% Er^{3+}/20 mol% Yb^{3+} ($x = 0$, 0.25, 0.5, 1, 0.75, and 1.25)

phosphors. The $Sc_2W_3O_{12}$ phosphors consist of a great number of small particles with a diameter of about 1 μm. The introduction of $(KMg)^{3+}$ ions causes an increase in crystallinity as well as grain growth. At $x = 0.25$, the phosphors consist of two phases with the appearance of a new $(KMg)_xSc_{2-x}W_3O_{12}$ structure. As the $(KMg)^{3+}$ ion substitution concentration increases, as shown in Fig. 3(c–e), the phosphors gradually transform into a pure $(KMg)_xSc_{2-x}W_3O_{12}$ phase and the grain size continues to grow to around 3–4 μm. However, with a further increase in the substitution concentration of $(KMg)^{3+}$ ions, short rod-shaped particles with a length of about 2 μm appear and are assigned to new impurity phase $MgWO_4$. As shown in Fig. S2 (ESI†), the EDX results show that Sc and K elements in the short rod-shaped particles are very low, while the content of the Mg element is relatively high. Thus, the short rod-shaped particles are predominantly $MgWO_4$, while large particles are hexagonal $(KMg)_xSc_{2-x}W_3O_{12}$. As shown in Fig. 3(g), clear lattice fringes can be observed in the high-resolution TEM (HRTEM) image and the interplanar spacing is about 0.407 nm, which is assigned to the (113) plane of the $(KMg)_{0.6}Sc_{1.4}W_3O_{12}$ phase. Fig. 3(f) shows the EDX results of the $(KMg)W_3O_{12}$:1 mol% Er^{3+}/20 mol% Yb^{3+} phosphors, which agree well with those of the target component.

The photoluminescence emission spectra of $(KMg)_ySc_{2-y}$-W_3O_{12}:1 mol% Eu^{3+} ($y = 0$, 0.25, 0.5, 0.75, 1, and 1.25)

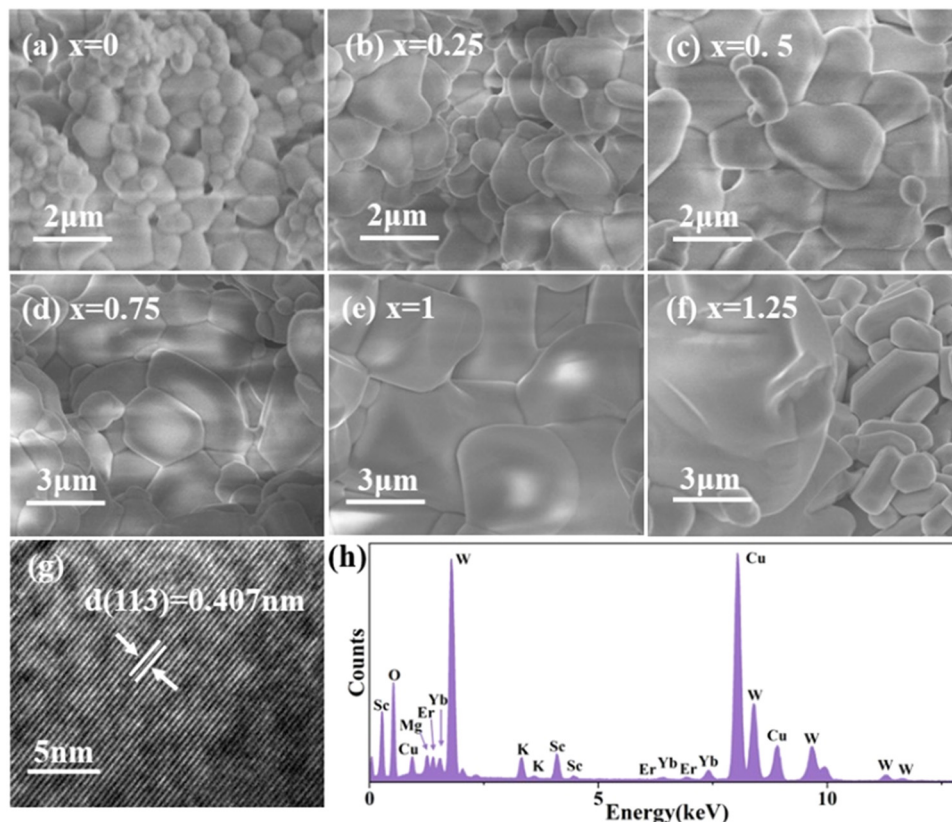**Fig. 3** (a)–(f) SEM images of $(KMg)_xSc_{2-x}W_3O_{12}$:1 mol% Er^{3+}/20 mol% Yb^{3+} (x = 0, 0.25, 0.5, 1, 0.75, and 1.25) phosphors. (g) HRTEM image and (h) EDX results of the $(KMg)ScW_3O_{12}$:1 mol% Er^{3+}/20 mol% Yb^{3+} phosphor.

phosphors are shown in Fig. 4(a). The emission peaks at 591 nm, 614 nm, 652 nm and 703 nm are attributed to $^5D_0 \rightarrow {}^7F_J$ (J = 1, 2, 3, 4) transitions of Eu^{3+}, respectively.[29] A dramatic change in the relative intensity of $^5D_0 \rightarrow {}^7F_2$ and $^5D_0 \rightarrow {}^7F_1$ transitions is observed, because their response to the local environmental change is completely different.[30] The intensity ratio β between $^5D_0 \rightarrow {}^7F_2$ and $^5D_0 \rightarrow {}^7F_1$ transition is usually considered as a criterion to assess the local symmetry of

the crystal structure and a larger value of β implies a lower lattice symmetry.[31] The gradual enlargement of the β value suggests that the local symmetry around Eu^{3+} reduces gradually, which is attributed to the structural distortion due to heterovalent doping and contributes to the enhancement of photoluminescence and temperature sensitivity.[32] The photoluminescence decay curves of $^5D_0 \rightarrow {}^7F_2$ transitions of Eu^{3+} ions under 460 nm excitation are shown in Fig. 5(b). All decay
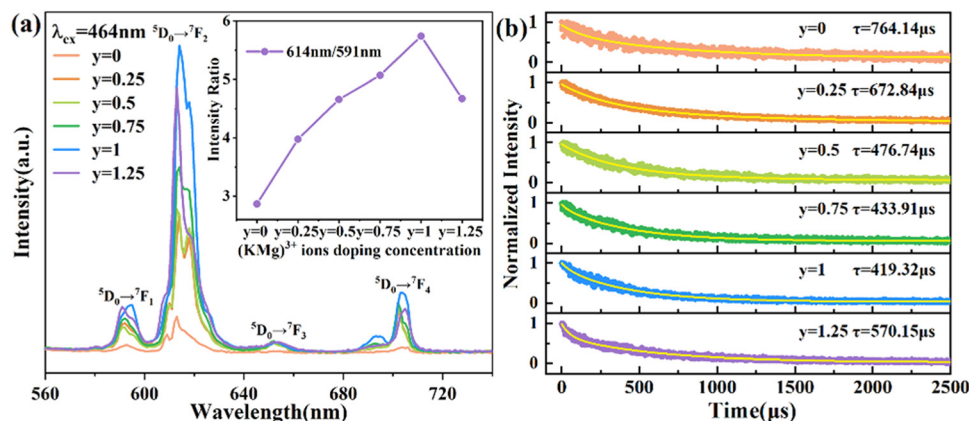

Fig. 4 (a) Photoluminescence emission spectra of $(KMg)_ySc_{2-y}W_3O_{12}$:1 mol% Eu^{3+} (y = 0, 0.25, 0.5, 0.75, 1, and 1.25) phosphors, inset: the intensity ratio β with different $(KMg)^{3+}$ concentrations. (b) Photoluminescence decay curves of Eu^{3+}:$^5D_0$.

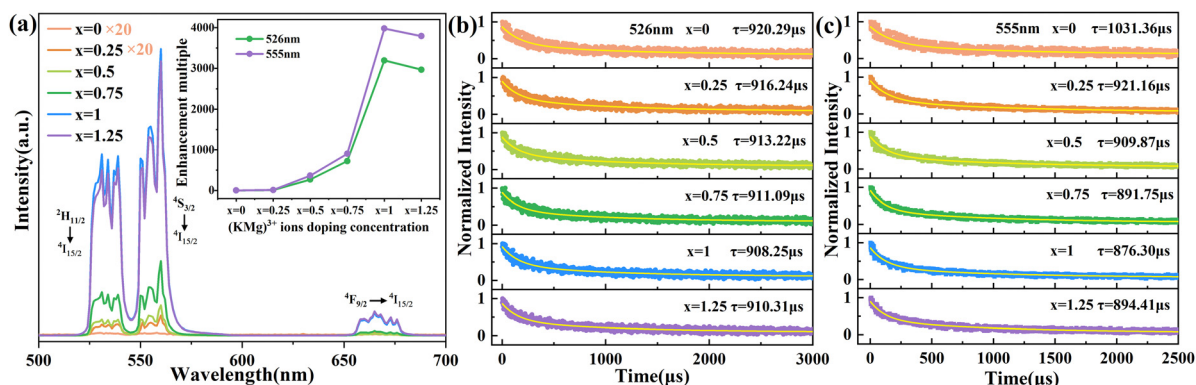**8980** | *J. Mater. Chem. C*, 2024, **12**, 8977–8986

This journal is © The Royal Society of Chemistry 2024

Fig. 5 (a) Upconversion emission spectra of $(KMg)_xSc_{2-x}W_3O_{12}$:1 mol% Er^{3+}/20 mol% Yb^{3+} (x = 0, 0.25, 0.5, 0.75, 1, and 1.25) phosphors, inset: multiple luminescence enhancement of the phosphor with different $(KMg)^{3+}$ concentrations. Photoluminescence decay curves of Er^{3+}: (b) $^2H_{11/2}$ and (c) $^4S_{3/2}$ in phosphors monitored at 370 nm.

curves of Eu^{3+}:$^5D_0$ can be well fitted into a two-exponent decay process, shown as follows:[33]

$$I(t) = M_1 \exp\left(\frac{-t}{\tau_1}\right) + M_2 \exp\left(\frac{-t}{\tau_2}\right) + N \qquad (1)$$

$$\tau = \frac{M_1\tau_1^2 + M_2\tau_2^2}{M_1\tau_1 + M_2\tau_2} \qquad (2)$$

where M_1, M_2, N are the fitting parameters, $I(t)$ is the luminous intensity of the phosphor at moment t, and τ is the lifetime decay. When the $(KMg)^{3+}$ ion doping concentration increases from y = 0 to y = 1, the average lifetime of Eu^{3+}:$^5D_0$ in $(KMg)_ySc_{2-y}W_3O_{12}$ phosphors decreases from 764.14 µs to 419.33 µs. It is well known that the lifetime τ is related to the radiative relaxation rate W_R, the non-radiative relaxation rate W_{NR} and the energy transfer rate W_{ET}, expressed as follows:[34]

$$\frac{1}{\tau} = W_R + W_{NR} + W_{ET} \qquad (3)$$

On the one hand, the reduced crystal field symmetry due to $(KMg)^{3+}$ impurity doping results in the increase of the transition probability of the energy level.[35,36] On the other hand, the smaller volume of $[(Mg/Sc)O_6]$ octahedra caused by the introduction of $(KMg)^{3+}$ ions leads to a reduction in the distance between Eu^{3+} ions and an increase in the energy transfer efficiency. Thus, the combination of the increased radiative relaxation rate and energy transfer efficiency results in a shorter lifetime and an enhanced luminescence. However, with a further increase in the $(KMg)^{3+}$ ion concentration, the average lifetime grows to 570.15 µs. This may be due to the presence of the $MgWO_4$ impurity phase, which leads to a renewed change in the lattice symmetry.

Fig. 5(a) displays the upconversion emission spectra of $(KMg)_xSc_{2-x}W_3O_{12}$:1 mol% Er^{3+}/20 mol% Yb^{3+} (x = 0, 0.25, 0.5, 0.75, 1, and 1.25) phosphors excited at 980 nm (power density: 0.5 W cm^{-2}). The green upconversion peaks at 526/ 555 nm correspond to the $^2H_{11/2}/^4S_{3/2} \rightarrow {}^4I_{15/2}$ transitions of Er^{3+} ions, respectively. The red upconversion peak at 660 nm corresponds to the $^4F_{9/2} \rightarrow {}^4I_{15/2}$ transition of Er^{3+} ions.[37]

The upconversion luminescence intensity continuously increases with the introduction of $(KMg)^{3+}$ ions and reaches the maximum value at x = 1. Compared to the $Sc_2W_3O_{12}$:Er^{3+}/Yb^{3+} phosphor, the integrated upconversion intensity of 526 and 555 nm in the $(KMg)ScW_3O_{12}$:Er^{3+}/Yb^{3+} phosphor was enhanced by factors of 3200 and 4000, respectively. To further investigate the influence of $(KMg)^{3+}$ ion substitution on Er^{3+} ion luminescence, the photoluminescence decay curves of $^2H_{11/2}/^4S_{3/2} \rightarrow {}^4I_{15/2}$ transitions were obtained and shown in Fig. 5(b) and (c). All curves of Er^{3+} ions could be fitted to a single exponential function, shown as follows:[38]

$$I(t) = M \exp\left(\frac{-t}{\tau}\right) + N \qquad (4)$$

in which M, N are the fitting parameters and τ is the lifetime decay. Apparently, the lifetimes of Er^{3+} ions have similar trends to those of Eu^{3+} ions.

The optimized Er^{3+}/Yb^{3+} doping concentration results are shown in Fig. 6(a) and (b) and the optimum concentrations are 2 mol% and 30 mol% for Er^{3+} and Yb^{3+} ions, respectively. XRD patterns (Fig. S4, ESI†) show that different Er^{3+}/Yb^{3+} co-doping concentrations have no significant effect on the structure of $(KMg)ScW_3O_{12}$ phosphors. The upconversion luminescence intensity values of the $(KMg)ScW_3O_{12}$:2 mol% Er^{3+}/30 mol% Yb^{3+} phosphor at different exciting powers were measured and shown in Fig. 6(c). The luminescence intensity increases with the increase of exciting power. The relationship between luminescence intensity (I) and exciting power (P) is in accordance with the following equation:

$$I \propto P^n \qquad (5)$$

in which n is expressed as the number of 980 nm photons absorbed when one upconversion photon is emitted. The relationship between $\log(I)$ and $\log(P)$ is displayed in the inset of Fig. 6(c). The slopes of upconversion luminescence at 526, 555 and 660 nm are 1.86, 1.80 and 1.82, respectively, which reveals that the mechanism of green-red upconversion luminescence is a double-photon absorption process. The possible upconversion mechanism of Er^{3+} and Yb^{3+} is plotted and
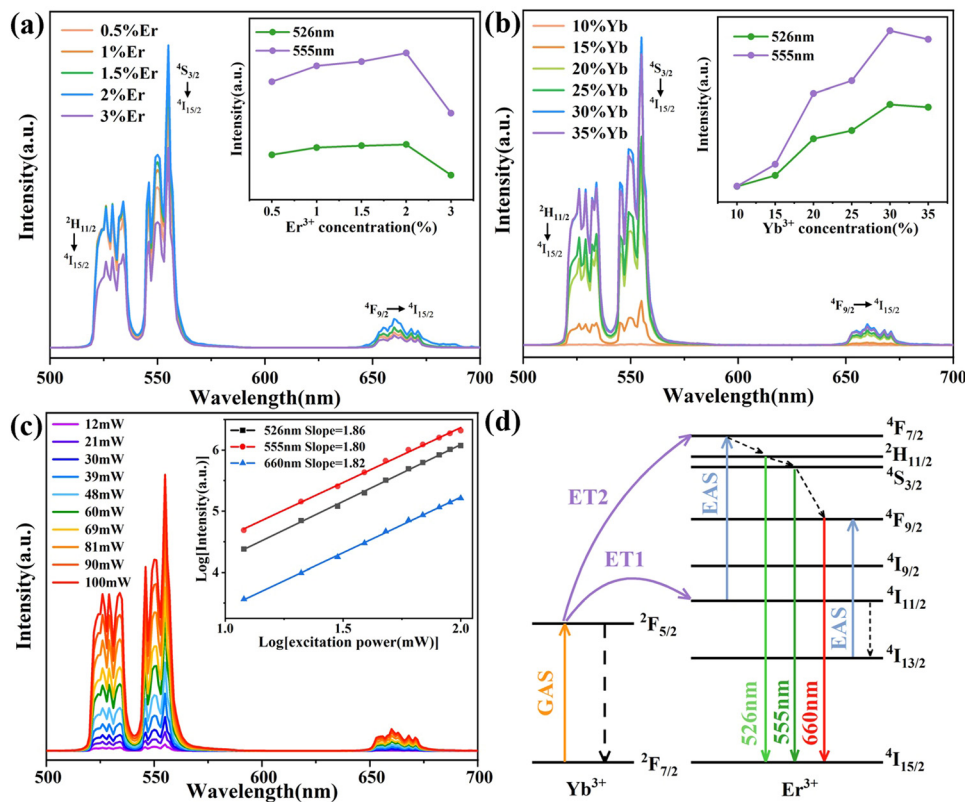
Fig. 6 Upconversion emission spectra of (a) (KMg)ScW$_3$O$_{12}$:a mol% Er^{3+}/20 mol% Yb^{3+} (a = 0.5, 1, 1.5, 2, and 3) and (b) (KMg)ScW$_3$O$_{12}$:2 mol% Er^{3+}/b mol% Yb^{3+} (b = 10, 15, 20, 25, 30, and 35). (c) Power-dependent upconversion emission spectra of the (KMg)ScW$_3$O$_{12}$:2 mol% Er^{3+}/30 mol% Yb^{3+} phosphor, inset: double log curve of exciting power and luminescence intensity. (d) The possible upconversion mechanism of Er^{3+} and Yb^{3+} ions.

shown in Fig. 6(d). Most of the 980 nm photons are absorbed by Yb^{3+} ions due to their high concentration and large absorption cross-section. The energy is rapidly transferred to the neighboring Er^{3+} ions.[37] Er^{3+} ions absorb the transferred energy and transition from $^4I_{15/2}$ to $^4I_{11/2}$. Subsequently, another 980 nm photon is absorbed by the Er^{3+} ion at the $^4I_{11/2}$ energy level and further excited to the $^4F_{7/2}$ energy level by the energy transfer (ET) process. Er^{3+} ions at the $^4F_{7/2}$ energy level rapidly relax to $^2H_{11/2}/^4S_{3/2}$ energy levels. Consequently, the radiative relaxation $^2H_{11/2}/^4S_{3/2} \rightarrow ^4I_{5/2}$ process occurs, generating green luminescence at 526 and 555 nm.

Fig. 7(a) displays the upconversion luminescence photographs of different phosphors (x = 0, Sc$_2$W$_3$O$_{12}$ and x = 1, (KMg)ScW$_3$O$_{12}$) at a power density of 0.5 W cm^{-2}. The upconversion intensity of both phosphors enhances as the temperature increases, which is similar to Liao's work.[19] At the same temperature, the upconversion luminescence brightness of the sample after impurity doping is much higher. Fig. 7(b) and (d) show the upconversion luminescence spectra and the integrated intensity of the Sc$_2$W$_3$O$_{12}$:2 mol% Er^{3+}/30 mol% Yb^{3+} phosphor at different temperatures. With the increase in temperature from 303 to 573 K, the upconversion intensity at 526 nm continuously increases, while the upconversion intensity at 555 nm increases and then decreases slightly. As shown in Fig. 7(c) and (e), similar trends are observed in the (KMg)ScW$_3$O$_{12}$:2 mol% Er^{3+}/30 mol% Yb^{3+} phosphor at

different temperatures and the phosphor exhibits a remarkable anti-quenching effect. It should be noted that, as shown in Fig. 7(f), the substitution of (KMg)$^{3+}$ for Sc^{3+} in the Sc$_2$W$_3$O$_{12}$ phosphor resulted in 3500-fold and 6000-fold enhancement of total green upconversion luminescence of Er^{3+} ions at room temperature and 573 K, respectively. The giant enhancement of anti-quenching upconversion luminescence in the (KMg)ScW$_3$O$_{12}$: 2 mol% Er^{3+}/30 mol% Yb^{3+} phosphor is attributed to the structural distortion caused by caused by impurity doping and the improved energy transfer efficiency caused by the NTE effect. In order to verify the existence of the NTE effect after heterovalent doping, the CTE curve of the (KMg)ScW$_3$O$_{12}$:2 mol% Er^{3+}/30 mol% Yb^{3+} sample is shown in Fig. 7(g). The CTE is -3.94×10^{-6} K^{-1} from room temperature to 573 K, which is slightly smaller than that of Sc$_2$W$_3$O$_{12}$ (with a CTE of -6×10^{-6} K^{-1} from 10 K to 1073 K[39]). It is widely recognized that the NTE properties originate from the lateral thermal motion of bridging oxygen atoms with increasing temperature, which leads to the mutual coupling and rotation of quasi rigid polyhedra, as well as lattice contraction. The reduction of NTE properties may be due to the fact that K$^+$ ions occupy the channel positions and limit the space for lateral thermal movement of the bridging oxygen atoms. The high-temperature XRD patterns are shown in Fig. 7(h). As the temperature increases, the diffraction peak shifts towards a higher angle, which further confirms the existence of NTE characteristics. The strong upconversion luminescence at room
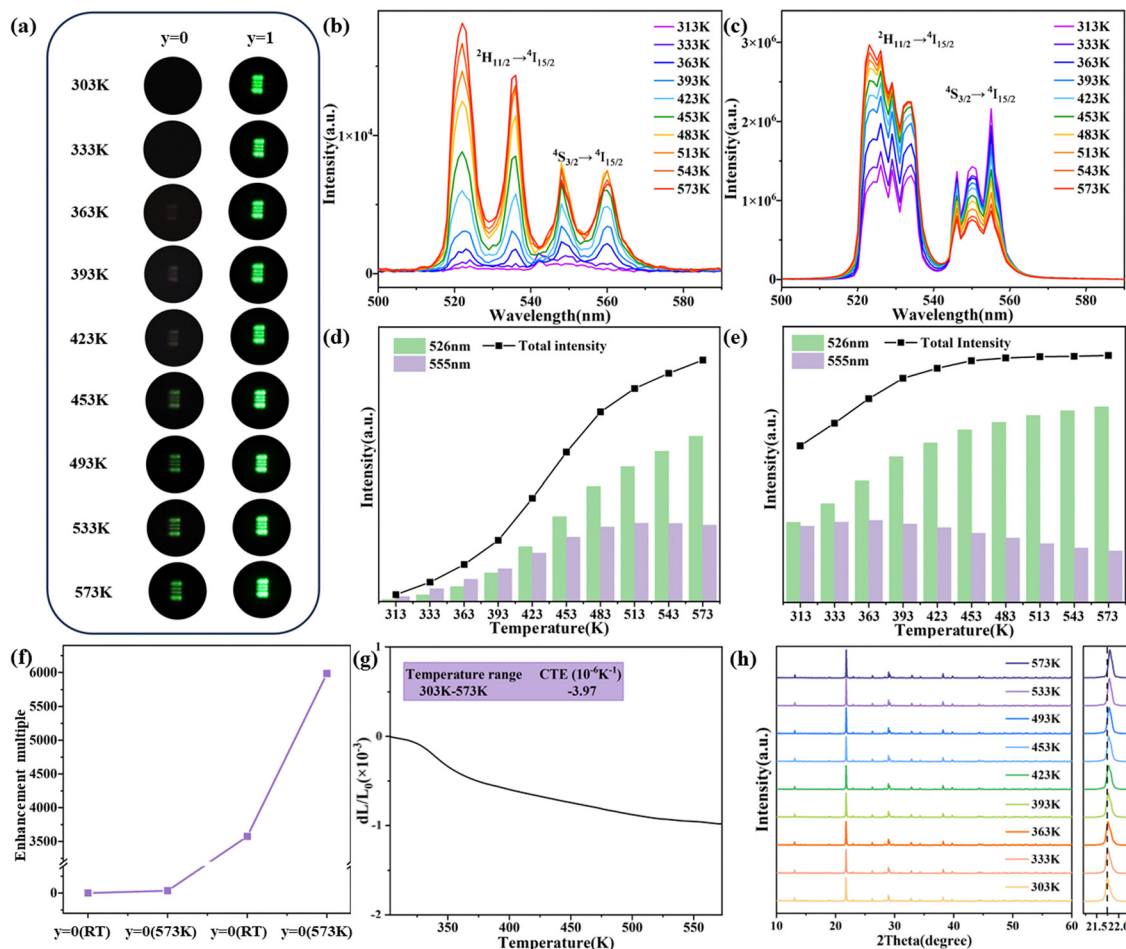
Fig. 7 (a) Upconversion luminescence photographs of both phosphors at various temperatures under 980 nm. The temperature-dependent green emission spectra of (b) $x = 0$ and (c) $x = 1$ phosphors. The temperature-dependent integrated upconversion intensity of (d) $x = 0$ and (e) $x = 1$ phosphors. (f) Multiple enhancement of green upconversion intensity of $x = 0$ at 573 K, $x = 1$ at RT and 573 K (power density: 0.5 W cm^{-2}). (g) CTE curves and (h) XRD patterns of the $x = 1$ phosphor from 303 K to 573 K.

temperature and high temperature after imuprity doping has laid a solid material foundation for the development of high-performance temperature sensors.

The temperature sensing performance of newly-developed (KMg)ScW$_3$O$_{12}$:2 mol% Er^{3+}/30 mol% Yb^{3+} phosphors is investigated based on the self-constructed all-fiber temperature sensing (AFTS) system (Fig. 8(a)). The system consists of a 980 nm laser, an optical isolator, a 1:99 optical splitter, a wavelength division multiplexer and a spectrometer connected by a single-mode fiber (SMF). The phosphors were cured with UV glue on the end-face of the SMF. The SEM image of the end-face of the SMF is displayed in Fig. 8(b). The phosphors located at the core position can be effectively excited by the 980 nm laser and emit bright green light (Fig. 8(c)).

The temperature-dependent upconversion emission spectra of the AFTS system and the corresponding integrated intensity at different temperatures are shown in Fig. S5 and S6 (ESI†), respectively. The excitation power of 980 nm laser is 1.25 mW. The variation trend of green upconversion luminescence is consistent with the above results (Fig. 7(c) and (e)). Because

^{2}H$_{11/2}$ and ^{4}S$_{3/2}$ of Er^{3+} ions are thermally coupled, their FIR follows the Boltzmann distribution equation. Fig. 9(a) shows the linear relationship between Ln(FIR) and $1/T$ with a fitted regression coefficient of 0.9996. The ultra-high regression coefficient indicates that the fitting result is very reliable and can be used as a standard curve for actual temperature measurement. In practical temperature measurements, absolute sensitivity (S_a) and relative sensitivity (S_r) are usually used to evaluate the temperature sensing performance of different optical materials. S_a is defined as the rate at which the FIR changes with temperature and can be calculated using the following equation:[40]

$$S_a = \frac{\mathrm{dFIR}}{\mathrm{d}T} = \mathrm{FIR}\left(\frac{\Delta E}{kT^2}\right) \qquad (6)$$

S_r is defined as the normalized S_a relative to FIR and can be calculated using:

$$S_r = \left|\frac{1}{\mathrm{FIR}} \times \frac{\mathrm{dFIR}}{\mathrm{d}T}\right| \times 100\% = \frac{\Delta E}{kT^2} \times 100\% \qquad (7)$$

This journal is © The Royal Society of Chemistry 2024

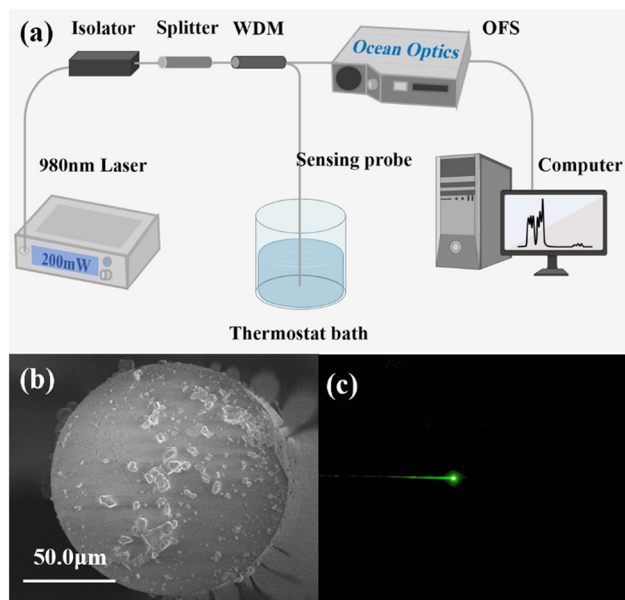*J. Mater. Chem. C*, 2024, **12**, 8977–8986 | **8983**

Fig. 8 (a) All-fiber optical temperature sensing system. (b) SEM image of the end-plane of the temperature probe. (c) Fluorescence photograph of the sensing probe at room temperature.

Fig. 9(b) shows the relationship between S_r, S_a and temperature. The value of S_a increases with the ambient temperature and the maximum value 0.0117 K^{-1} is achieved at 423 K. A gradual decrease of the S_r value with the increasing

temperature is observed and the maximum value 0.0165 K^{-1} is achieved at 253 K. As shown in Table S1 (ESI†), these temperature sensing results are comparable to the previously reported results for the $A_2M_3O_{12}$ material with the same structure.

The stability of the AFTS system was evaluated by 60 parallel tests at 293 K, 313 K, 333 K and 353 K with an interval of 15 seconds. Fig. 9(c) shows the calculated FIR values. The almost unchanged FIR values indicate that the whole AFTS system is dependable and the thermal effect of continuous irradiation 980 nm laser is almost completely negligible. According to the calibration curve shown in Fig. 9(a), the corresponding temperature was obtained and presented in Fig. 9(d). Most of the points have very small temperature fluctuations with a temperature deviation (ΔT) of ± 0.3 K. The above results show that the AFTS system has excellent temperature stability, high sensitivity and anti-interference properties.

The AFTS system is then used for real-time temperature monitoring of the CPU chip and the results are shown in Fig. 10(a). A thermocouple thermometer (KAIPUSEN YET610L) was employed to verify the reliability of temperature measurement. The sensing probe and thermocouple were tightly attached on the surface of a CPU chip using thermally conductive silicone grease. The temperature of the CPU chip varied through Fur Mark GPU stress test software. The temperature increases as the software operates, and the FIR of the sensing probe changes immediately, as shown in Fig. S7 (ESI†). Fig. 10(b) displays the real-time temperature variations for six cycles measured using the AFTS system and the thermocouple. The trend of temperature changes
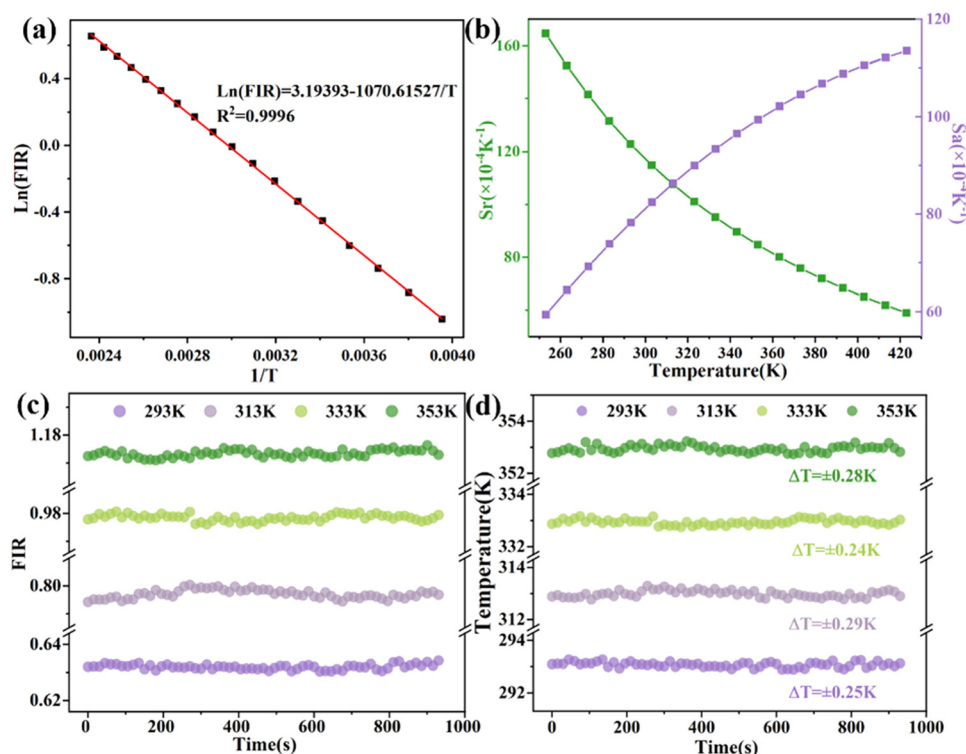

Fig. 9 (a) The relationship between Ln(FIR) and $1/T$. (b) Absolute sensitivity and relative sensitivity of (KMg)ScW$_3$O$_{12}$ phosphor dependence on temperature. (c) Calculated FIR values at 293 K, 313 K, 333 K and 353 K. (d) Corresponding temperature and ΔT recorded at 293 K, 313 K, 333 K and 353 K.

8984 | *J. Mater. Chem. C*, 2024, **12**, 8977–8986

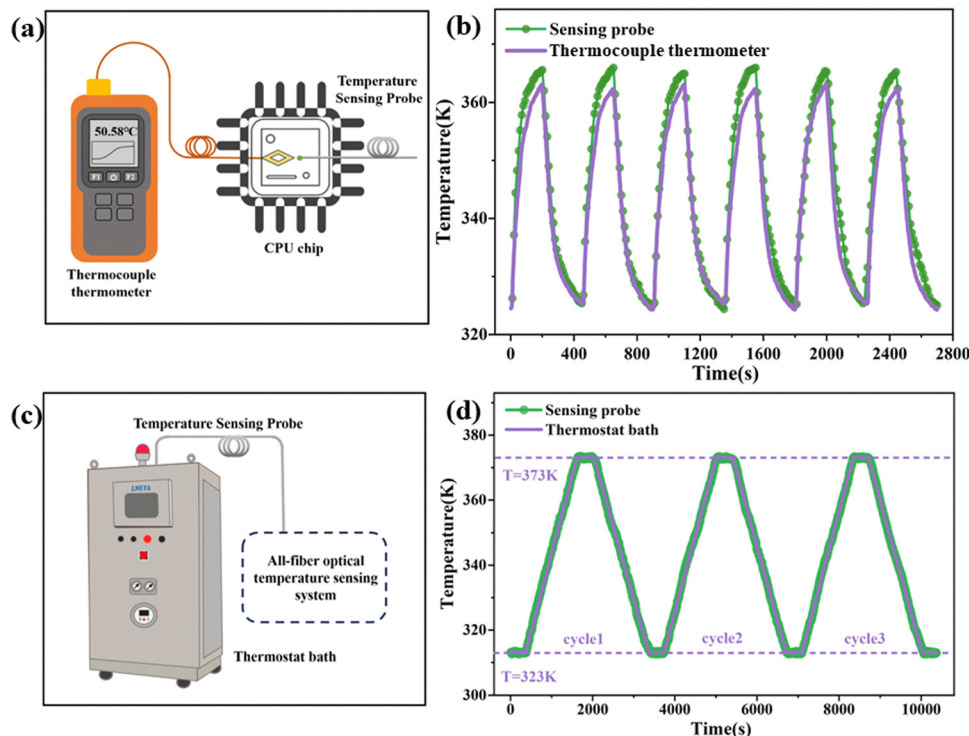This journal is © The Royal Society of Chemistry 2024

Fig. 10 (a) Schematic diagram of CPU temperature measurement. (b) The real-time temperature variation of CPU. (c) Schematic diagram of thermostat bath temperature measurement. (d) The real-time temperature variation of the thermostat bath.

is almost completely synchronous and the temperature of six cycles is very stable. Especially, the real-time temperature above 350 K measured using the AFTS system is higher than that measured using the thermocouple. The fast response of the AFTS system can better reflect the real-time temperature changes of the CPU chip in real time, while a significant hysteresis effect on temperature change is observed for the thermocouple. Temperature monitoring is crucial in chemical production and reactions. Accurate temperature monitoring in real-time is essential for chemical production and reaction, and thermostat baths are extensively used to provide a stable temperature environment or achieve different temperature gradients. The AFTS system is also used for the temperature measurements of the thermostat bath and the schematic is shown in Fig. 10(c). The FIR fitting curve is shown in Fig. S8 (ESI†) with a fitted regression coefficient of 0.9997. Three cycles of the temperature rise and fall process were carried out from 323 K to 373 K. The real-time temperature was measured simultaneously using the thermostat bath and AFTS system and the results are shown in Fig. 10(d). The temperature measured using the AFTS system is in excellent agreement with the temperature measured using the the thermostat, demonstrating the accuracy of the temperature monitoring. Therefore, the temperature sensor has great potential for temperature monitoring in real-time industrial production.

4 Conclusions

The gradual substitution of $(KMg)^{3+}$ for Sc^{3+} in $Sc_2W_3O_{12}$ phosphors causes the transition of the crystal phase from orthorhombic $Sc_2W_3O_{12}$ to hexagonal $(KMg)_{2-x}Sc_xW_3O_{12}$. The structural distortion and the reduction of the maximum phonon energy due to impurity doping result in a factor of 3200 and 4000 enhancement for 526 nm and 555 nm green upconversion luminescence of Er^{3+} ions at room temperature. Anomalous anti-quenching green upconversion luminescence was observed in the $(KMg)ScW_3O_{12}$:Er^{3+}/Yb^{3+} phosphor attributed to its NTE properties. Compared with the $Sc_2W_3O_{12}$:Er^{3+}/Yb^{3+} phosphor at room temperature, the upconversion intensity of the $(KMg)ScW_3O_{12}$:Er^{3+}/Yb^{3+} phosphor at 573 K increases by 6000 times. The temperature sensing characteristics were investigated using an all-fiber temperature sensing platform based on the FIR technology. Intense green upconversion signals were recorded in the entire temperature measurement range of 253–423 K, which shows that accurate temperature sensing is achieved. The maximum relative sensitivity of 0.0165 K^{-1} was reached at 253 K. A small temperature error (± 0.3 K) and good repeatability indicate that the AFTS system is reliable. The real-time temperature monitoring of a CPU chip and a thermostat bath was successfully demonstrated.

Conflicts of interest

There are no conflicts to declare.

Acknowledgements

This journal is © The Royal Society of Chemistry 2024

J. Mater. Chem. C, 2024, **12**, 8977–8986 | **8985**

References

1 X.-d Wang, O. S. Wolfbeis and R. J. Meier, *Chem. Soc. Rev.*, 2013, **42**, 7834–7869.

2 M. Ding, M. Xu and D. Chen, *J. Alloys Compd.*, 2017, **713**, 236–247.

3 Q. Wang, M. Liao, Q. Lin, M. Xiong, Z. Mu and F. Wu, *J. Alloys Compd.*, 2021, **850**, 156744.

4 Y. Cheng, Y. Gao, H. Lin, F. Huang and Y. Wang, *J. Mater. Chem. C*, 2018, **6**, 7462–7478.

5 M. Liu, Q. Wan, H. Wang, F. Carulli, X. Sun, W. Zheng, L. Kong, Q. Zhang, C. Zhang, Q. Zhang, S. Brovelli and L. Li, *Nat. Photonics*, 2021, **15**, 379–385.

6 J. Qiao, L. Ning, M. S. Molokeev, Y.-C. Chuang, Q. Liu and Z. Xia, *J. Am. Chem. Soc.*, 2018, **140**, 9730–9736.

7 H. Chen, D. Li, L. Zhang, G. Bai, S. Xu and L. Chen, *J. Appl. Phys.*, 2021, **129**, 143101.

8 J. Huang, Z. Han, B. Fu, H. Yan, J. Liao, G. Gong and H.-R. Wen, *Mater. Today Commun.*, 2022, **33**, 104548.

9 Q. Wang, J. Wen, J. Zheng, Q. Xia, C. Wei, X. Huang, Z. Mu and F. Wu, *J. Lumin.*, 2022, **252**, 119306.

10 H. Zheng, B. Chen, H. Yu, X. Li, J. Zhang, J. Sun, L. Tong, Z. Wu, H. Zhong, R. Hua and H. Xia, *Sens. Actuators, B*, 2016, **234**, 286–293.

11 M.-Y. Wu, Y. Jia and Q. Sun, *Comput. Mater. Sci.*, 2016, **111**, 28–33.

12 P. I. P. Bojan, A. Marinkovic, C. P. Romao, T. Moreira and M. Anne White, *Front. Mater.*, 2011, **8**, 741560.

13 H. F. Liu, Y. J. Wang, Z. P. Zhang, J. Zhu, W. Wang and X. H. Zeng, *J. Alloys Compd.*, 2023, **966**, 171481.

14 Z. P. Zhang, Y. Wang, W. Wang and H. F. Liu, *Int. J. Appl. Ceram. Technol.*, 2022, **19**, 2322–2330.

15 Y. G. Cheng, X. S. Liu, W. B. Song, B. H. Yuan, X. L. Wang, M. J. Chao and E. J. Liang, *Mater. Res. Bull.*, 2015, **65**, 273–278.

16 S. S. Nanda, P. Nayak, S. Pattnaik, V. K. Rai and S. Dash, *J. Alloys Compd.*, 2023, **934**, 167732.

17 H. Liang, Y. Zheng, G. Chen, L. Wu, Z. Zhang and W. Cao, *J. Alloys Compd.*, 2011, **509**, 409–413.

18 S. Sinha, A. Mondal, K. Kumar and H. C. Swart, *J. Alloys Compd.*, 2018, **747**, 455–464.

19 J. Liao, M. Wang, F. Lin, Z. Han, B. Fu, D. Tu, X. Chen, B. Qiu and H.-R. Wen, *Nat. Commun.*, 2022, **13**, 2090.

20 Z. Hua, J. Liu and X. Yan, *Bull. Chin. Ceram. Soc.*, 2010, **29**, 8.

21 H. Liu, W. Sun, Z. Zhang, L. N. Lovings and C. Lind, *Solids*, 2021, **2**, 87–107.

22 M. K. Gupta, R. Mittal and S. L. Chaploe, *J. Appl. Phys.*, 2019, **126**, 125114.

23 W. Paraguassu, M. Maczka, A. G. S. Filho, P. T. C. Freire, F. E. A. Melo, J. M. Filho and J. Hanuza, *Vib. Spectrosc.*, 2007, **44**, 69–77.

24 A. Kar, S. Kundu and A. Patra, *ChemPhysChem*, 2015, **16**, 505–521.

25 W. You, D. Tu, W. Zheng, P. Huang and X. Chen, *J. Lumin.*, 2018, **201**, 255–264.

26 N. Garg, C. Murli, A. K. Tyagi and S. M. Sharma, *Phys. Rev. B: Condens. Matter Mater. Phys.*, 2005, **72**, 064106.

27 H. Liu, Y. Wang and Z. Zhang, *Ceram. Int.*, 2022, **48**, 16554–16561.

28 H. Yin, X. Zhang, L. Li, J. Zhang and R. Ding, *J. Rare Earths*, 2021, **11**, 1344–1352.

29 K. Binnemans, *Coord. Chem. Rev.*, 2015, **295**, 1–45.

30 L. Zeng, M. Song, D. Chen, H. Zhou, Y. Liu, J. Zeng, G. Liu, J. Jian, Z. Yuan, Z. Li, J. Xu, C. Xu and J. Tang, *Ceram. Int.*, 2019, **45**, 19730–19736.

31 L. Chen, P. Cheng, Z. Zhang, L. He, Y. Jiang, G. Li, X. Jing, Y. G. Qin, M. Yin, T.-S. Chan, B. Hong, S. Tao, W. Chu, Z. Zhao, H. Ni, H. Kohlmann and O. Oeckler, *Adv. Sci.*, 2019, **6**, 1970096.

32 Z. Zou, T. Wu, H. Lu, Y. Tu, S. Zhao, S. Xie, F. Han and S. Xu, *RSC Adv.*, 2018, **8**, 7679–7686.

33 H. Yi, F. Li, L. Wu, L. Wu and J. Xu, *RSC Adv.*, 2014, **4**, 64244–64251.

34 Y. Zheng, B. Chen, H. Zhong, J. Sun, L. Cheng, X. Li, J. Zhang, Y. Tian, W. Lu, J. Wan, T. Yu, L. Huang, H. Yu and H. Lin, *J. Am. Ceram. Soc.*, 2011, **94**, 1766–1772.

35 A. Kumari, A. Pandey, R. Dey and V. K. Rai, *Rsc Adv*, 2014, **4**, 21844–21851.

36 S. K. Gupta, K. Sudarshan, A. K. Yadav, R. Gupta, D. Bhattacharyya, S. N. Jha and R. M. Kadam, *Inorg. Chem.*, 2018, **57**, 821–832.

37 H. Dong, L.-D. Sun and C.-H. Yan, *Chem. Soc. Rev.*, 2015, **44**, 1608–1634.

38 R. Cao, H. Xu, W. Luo, Z. Luo, S. Guo, F. Xiao and H. Ao, *Mater. Res. Bull.*, 2016, **81**, 27–32.

39 J. S. O. Evans, T. A. Mary and A. W. Sleight, *J. Solid State Chem.*, 1998, **137**, 148–160.

40 Y. Tian, Y. Tian, P. Huang, L. Wang, Q. Shi and C. E. Cui, *Chem. Eng. J.*, 2016, **297**, 26–34.

8986 | *J. Mater. Chem. C*, 2024, **12**, 8977–8986

This journal is © The Royal Society of Chemistry 2024